Confinement and bound states of bound states in a transverse-field two-leg Ising ladder

Flávia B. Ramos [1], Máté Lencsés [2,3] J. C. Xavier [4], and Rodrigo G. Pereira [1,5]

[1]*International Institute of Physics, Universidade Federal do Rio Grande do Norte, Natal, RN, 59078-970, Brazil*
[2]*BME Department of Theoretical Physics, H-1111 Budapest, Budafoki út 8, Hungary*
[3]*BME Momentum Statistical Field Theory Research Group, H-1111 Budapest, Budafoki út 8, Hungary*
[4]*Universidade Federal de Uberlândia, Instituto de Física, C. P. 593, 38400-902 Uberlândia, MG, Brazil*
[5]*Departamento de Física Teórica e Experimental, Universidade Federal do Rio Grande do Norte, Natal, RN, 59078-970, Brazil*

Weakly coupled Ising chains provide a condensed-matter realization of confinement. In these systems, kinks and antikinks bind into mesons due to an attractive interaction potential that increases linearly with the distance between the particles. While single mesons have been directly observed in experiments, the role of the multiparticle continuum and bound states of mesons in the excitation spectrum is far less clear. Using time-dependent density-matrix renormalization group methods, we study the dynamical structure factors of one- and two-spin operators in a transverse-field two-leg Ising ladder in the ferromagnetic phase. The propagation of time-dependent correlations and the two-spin excitation spectrum reveal the existence of interchain bound states, which are absent in the one-spin dynamical structure factor. We also identify two-meson bound states that appear at higher energies, above the thresholds of several two-meson continua.

I. INTRODUCTION

Over the last few decades, the phenomenon of confinement has attracted considerable interest in both theoretical and experimental condensed-matter physics [1–27]. Akin to quark confinement via the strong force in quantum chromodynamics (QCD), the elementary excitations of some quasi-one-dimensional magnets form bound states due to interacting potentials that increase with the distance between the particles. As a consequence, free particles cannot be directly observed in the excitation spectrum. Well-established examples include the ferromagnetic Ising chain in a weak longitudinal field, the antiferromagnetic XXZ chain with an easy-axis staggered field [4–8], and weakly coupled chains [12–23]. In the Ising chain, for instance, the elementary excitations in the ordered phase are kinks in the magnetization profile, and the external longitudinal field creates a linear potential that binds kinks and antikinks. We shall refer to such bound states as mesons, in analogy with bound states of a quark and an antiquark in QCD. Even in the absence of an external magnetic field, a finite interchain coupling plays the role of the confining potential [13]. In addition, confined states arise in the transverse-field Ising chain with long-range interactions [8,24–26] and in 1+1 dimensional quantum electrodynamics [28,29].

Hallmark signatures of confinement can be observed in dynamical properties of quantum many-body systems in real time as well as in the frequency domain. In the real-time domain, even a weak confining potential has been shown to lead to dramatic changes in quench dynamics, such as nonthermalization, strong suppression of the light cone that bounds the propagation of correlations, and multifrequency oscillations in the entanglement entropy and one-point functions [6–11]. The time evolution after quantum quenches can be experimentally probed in quantum simulators, see for example Refs. [30–34].

Recently, confinement dynamics was realized in trapped ions that simulate an Ising-like chain with long-range interactions [26] and on an IBM quantum computer [35]. In the frequency domain, confinement in magnetic systems can be inferred from the analysis of dynamical structure factors (DSFs), which relate to inelastic scattering cross sections and absorption spectra directly measured in experiments. From this perspective, the formation of mesons is manifested as a discrete spectrum that contrasts with the two-particle continuum of the unconfined system [1]. Evidence of confinement was observed in quasi-one-dimensional compounds such as $CaCu_2Co_3$ [14], $CoNb_2O_6$ [15,16], $BaCo_2V_2O_8$ [18–20], $SrCo_2V_2O_8$ [21,22], and Yb_2Pt_2Pb [23].

In all these materials, the confinement of the elementary excitations is an intrinsic property that arises due to the interchain coupling. Being weak, the interchain coupling is often treated within a mean-field approximation as an effective magnetic field proportional to the local magnetization [13]. This approximation leaves out the interesting possibility of multiparticle excitations where bound states form not only between kinks within the same chain, but also between adjacent chains. At weak coupling, such interchain bound states can occur in transitions promoted by two-spin operators that act on different chains simultaneously. While inelastic neutron scattering is described by one-spin DSFs [14,15], excitations associated with two-spin operators contribute to the cross section in resonant inelastic x-ray scattering [36,37] and to the optical conductivity below the Mott gap [38] measured by terahertz spectroscopy [16,21].

In this paper, we investigate the formation of mesons and multiparticle bound states in weakly coupled transverse-field Ising chains beyond the mean-field approximation for the interchain coupling. For this purpose, we analyze the DSFs of one- and two-spin operators for a two-leg ladder in the

ferromagnetic phase. Since the ladder model is nonintegrable, we use numerical techniques to compute the physical quantities of interest. To determine the ground-state phase diagram of the system, we apply the density-matrix renormalization group (DMRG) [39] and truncated fermionic space approach (TFSA) [40]. We also apply state-of-the-art time-dependent density-matrix renormalization group (tDMRG) methods [41] to compute the dynamical properties. We interpret our results in terms of the semiclassical picture of massive particles moving in the presence of a linear interaction potential. In addition to the mesons observed in the dynamics of ferromagnetic Ising chains, our high-resolution results show that the two-leg Ising ladder harbors additional bound states that are not allowed in a single chain due to the fermionic nature of the kinks. Furthermore, we find peaks above two-meson continua which we ascribe to two-meson bound states formed due to a repulsive meson-meson interaction.

This paper is organized as follows. In Sec. II, we describe the ground-state phase diagram of the two-leg Ising ladder. In addition, we present a discussion of the quantum critical line in terms of the scaling field theory. In Sec. III, we discuss the semiclassical problem of two massive particles in a linear potential. In Sec. IV, we present our tDMRG results for three different DSFs that allow us to assess the role of intra- and interchain bound states. Finally, we provide concluding remarks in Sec. V.

II. MODEL AND PHASE DIAGRAM

The Hamiltonian of the ferromagnetic two-leg Ising ladder in a transverse magnetic field is

$$H = -J \left[\sum_{j,\alpha} \left(\sigma^x_{\alpha,j} \sigma^x_{\alpha,j+1} + h_z \sigma^z_{\alpha,j} \right) + \lambda \sum_j \sigma^x_{1,j} \sigma^x_{2,j} \right], \quad (1)$$

where $\sigma^{x,z}_{\alpha,j}$ are Pauli spin operators acting on site j of leg $\alpha = 1, 2$, J is the intrachain exchange coupling, $h_z J$ is the transverse magnetic field, and λJ is the interchain coupling. Throughout this paper, we assume $\lambda, h_z \geqslant 0$ and set the energy scale $J = 1$ in the numerical results.

For $\lambda = 0$, the system consists of two decoupled transverse field Ising models (TFIMs). The TFIM is exactly solvable by mapping, via a Jordan-Wigner transformation, to free fermions with the dispersion relation [42]

$$\varepsilon(k) = 2J\sqrt{(h_z - \cos k)^2 + \sin^2 k}. \quad (2)$$

In this case, the model in Eq. (1) exhibits a $\mathbb{Z}_2 \times \mathbb{Z}_2$ symmetry corresponding to an invariance under flipping all the spins in the same chain, $\sigma^x_{\alpha,j} \mapsto -\sigma^x_{\alpha,j} \ \forall j$. The ground-state phase diagram for each decoupled chain is characterized by two phases separated by a quantum critical point at $h_z = 1$. For $h_z < 1$, the system is ferromagnetically ordered and the ground state has a twofold degeneracy for each decoupled chain. In this case, the symmetry is spontaneously broken and the order parameter corresponds to the magnetization along the longitudinal direction, $\langle \sigma^x_{\alpha,j} \rangle \neq 0$. On the other hand, for $h_z > 1$, the system is in the paramagnetic phase with unbroken symmetry. A well-known extension of the TFIM
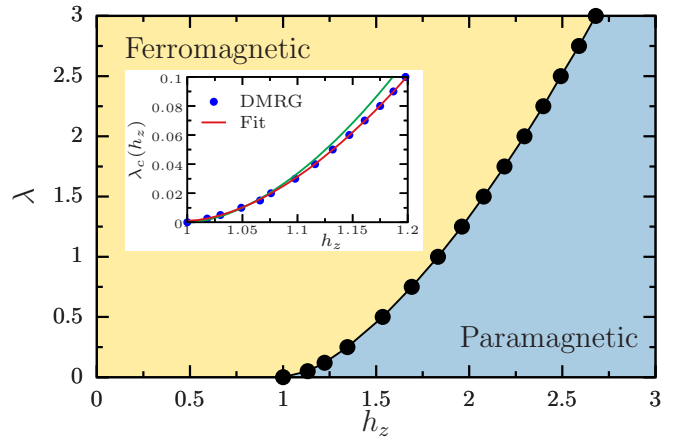

FIG. 1. Ground-state phase diagram of the two-leg Ising ladder as a function of the interchain coupling λ and the transverse magnetic field h_z. The filled circles are the DMRG points and the black solid line, which connects those points, is the phase transition line separating the ferromagnetic phase (in yellow) from the paramagnetic phase (in blue). The inset shows the fit of our numerical results in the interval $0 \leqslant \lambda \leqslant 0.1$ using $\lambda_c(h_z) = A(h_z - h_0)^\beta$. The estimates of the exponent β and the coefficient A are 1.8 and 1.7, respectively. The solid green line is the field-theory prediction $\lambda_c(h_z) = 1.89(h_z - 1)^{7/4}$.

involves switching on a longitudinal field h_x, in which case the symmetry of the Hamiltonian is explicitly broken and the ground state is unique for any h_z. The evolution of the elementary excitations on the h_z-h_x plane is complicated, but there are no additional critical points [2,40,43].

The situation is quite different in the case of the ladder. Switching on the interchain coupling, $\lambda \neq 0$, lowers the symmetry from $\mathbb{Z}_2 \times \mathbb{Z}_2$ to a single $\mathbb{Z}_2$. The limit $\lambda \gg 1$ is particularly simple, as the effective Hamiltonian in the low-energy subspace is a single Ising chain with parallel spins in each rung. In fact, the ground-state phase diagram of the two-leg Ising ladder presents a phase transition line $\lambda_c(h_z)$ in the Ising universality class, starting from the critical point $\lambda = 0$, $h_z = 1$. This quantum critical line separates a ferromagnetic from a paramagnetic phase on the whole h_z-λ plane [44]. Analogously to the TFIM, the remaining $\mathbb{Z}_2$ symmetry is spontaneously broken in the ferromagnetic phase and the ground state is twofold degenerate. Meanwhile, the symmetry is preserved in the paramagnetic phase with a unique ground state.

The quantum critical line can be accurately determined by analyzing the scaling behavior of the entanglement entropy [45]. Following the procedure reported in Ref. [45], we use DMRG to obtain the finite-size estimates $\lambda_c(h_z, L)$, where L is the length of the ladder with open boundary conditions. To obtain $\lambda_c(h_z)$ in the thermodynamic limit, we assume that $\lambda_c(h_z, L)$ behaves as $\lambda_c(h_z, L) = \lambda_c(h_z) + a/L + b/L^2$. We then estimate $\lambda_c(h_z)$ from the fit of the numerical data considering system sizes $L = 40, 60, 80, 100$, and $L = 200$. The result for the critical line is shown in Fig. 1. Estimates of critical transverse fields were obtained for the isotropic ($\lambda = 1$) N-leg Ising ladders using the same method [46].

Let us now discuss the model from the scaling field theory point of view. For $\lambda = 0$ and $h_z = 1$, the system can be described by conformal field theory (CFT) [47]. In this case, the CFT fixed point is a product of two Ising fixed points with scaling fields $\mathbf{1}_\alpha, \epsilon_\alpha, \sigma_\alpha$, with $\alpha = 1, 2$ being the leg index, corresponding to the identity, energy density, and spin density, respectively. The respective conformal weights $(h, \bar{h})$ of these fields are $(0,0)$, $(1/2, 1/2)$, and $(1/16, 1/16)$. In this context, for $|h_z - 1| \ll 1$ and $|\lambda| \ll 1$, the ladder can be described by the following Euclidean action:

$$S = S_1^{\mathrm{CFT}} + S_2^{\mathrm{CFT}} + \frac{m}{2\pi} \int d^2x(\epsilon_1 + \epsilon_2) + \tilde{\lambda} \int d^2x \sigma_1 \sigma_2,$$

$$(3)$$

where $m = 2J(1 - h_z)$ is the mass and $\tilde{\lambda} = (2/\bar{s}^2)J^{7/4}\lambda$ is the rescaled interchain coupling, where $\bar{s} = 2^{1/12}e^{-1/8}\mathcal{A}^{3/2}$ with Glaisher's constant $\mathcal{A} = 1.2824271291\ldots$ [48]. For convenience, we define the dimensionless (renormalization-group invariant) combination $\eta \equiv \tilde{\lambda}^{4/7}/|m|$.

The spin-spin coupling in Eq. (3) was studied in Ref. [49]. The phase transition with both the mass term and the spin-spin coupling can be captured in the field theory as predicted in the context of the two-frequency sine-Gordon model [44] and later analyzed in Refs. [50,51]. However, to the best of our knowledge, this has not been studied from the point of view of the coupled Ising field theory. Starting from the paramagnetic phase with a given mass, say $|m| = 1$, one hits the phase transition line ($\eta = \eta_c$) by increasing the interchain coupling. In the paramagnetic phase with $\eta < \eta_c$, the ground state is unique. The low-energy spectrum of a system with finite volume R exhibits a mass gap with small exponential corrections in R. At the critical point, the energy levels of the finite-volume system scale with $1/R$. Finally, for $\eta > \eta_c$ in the ferromagnetic phase, the ground state is twofold degenerate up to an exponentially small energy splitting. The evolution of the finite-size spectrum with increasing η can be analyzed using the tensor product extension of the TFSA [40]. Using TFSA, we have obtained $\tilde{\lambda}_c \approx 0.61$ for $|m| = 1$. In addition, we are able to identify the low-lying spectrum of the Ising fixed point (see Fig. 2).

Based on the above scaling field theory arguments, one can fit the DMRG data using $\lambda_c(h_z) = A(h_z - h_0)^\beta$. The exact critical field at $\lambda = 0$ is $h_0 = 1$. The exact exponent $\beta = 7/4$ is fixed by the scaling dimensions of the fields, via the relation with the renormalization-group-invariant parameter η. In addition, using the rescaled critical coupling $\tilde{\lambda}_c \approx 0.62$ for $|m| = 1$, we extract the coefficient $A_{\mathrm{TFSA}} \approx 1.89$ from TFSA data. By performing a fit of the DMRG results using the interval $\lambda \in [0.025, 0.09]$, we obtain $\beta_{\mathrm{DMRG}} \approx 1.8$, $A_{\mathrm{DMRG}} \approx 1.7$ and $h_0^{\mathrm{DMRG}} \approx 0.99$ (see the inset in Fig. 1). We note that the fitted exponent varies by about 5% and the prefactor by about 10% if we choose different intervals in the range $\lambda \in [0, 0.1]$. Since the values of $h_z - 1$ used here are not exceptionally small, we believe that more robust and precise fitting parameters could be obtained by incorporating higher-order corrections, associated with irrelevant operators in the field theory, to the expression for $\lambda_c(h_z)$. Note that in the vicinity of the Ising critical point, $|h_z - 1| \ll 1$, our results show remarkable agreement with the field-theory prediction.
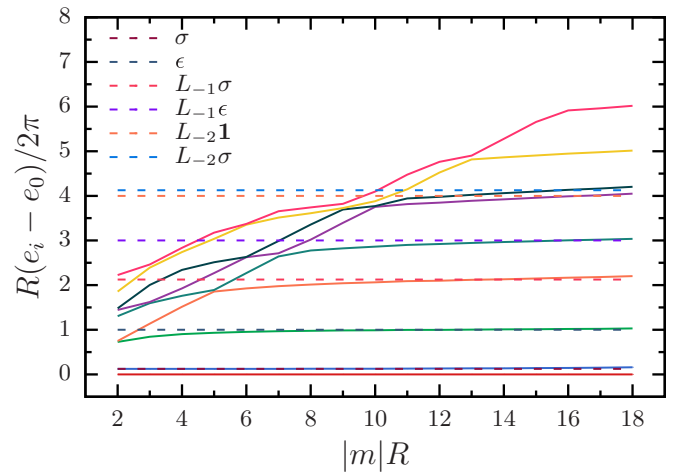

FIG. 2. The rescaled energy gaps $R(e_i - e_0)/(2\pi)$ at $|m| = 1$ and $\tilde{\lambda} = 0.61$ against the dimensionless volume $|m|R$ from TFSA. The dashed horizontal lines show the weights of low-lying Ising CFT states. Here L_{-n} are Virasoro generators. Note that for larger volumes and higher states, the TFSA is less reliable due to truncation errors [52–55]. The lines with slopes are related to the high-energy spectrum and they do not play any role in the phase transition.

III. SEMICLASSICAL SOLUTION

We now focus on the low-energy excitations of the ferromagnetic two-leg Ising ladder in the regime of weak interchain coupling. For comparison with the tDMRG results in Sec. IV, in the following we discuss the confinement effect based on the mean-field theory picture and the analogy of the Ising ladder with the TFIM in a weak longitudinal magnetic field.

Let us recall the basic phenomenology of confinement in the Ising chain [1,2,4]. In the absence of a longitudinal field, the ferromagnetic Ising chain has two degenerate ground states, and the elementary excitations of the system are free domain walls (kinks) interpolating between them. For small but finite h_x, the degeneracy is broken and an energy-density difference between the two ground states is observed, so that one of them becomes a "false" one. If we imagine a two-kink configuration on a "true" ground-state background, it is clear that it acquires additional energy proportional to the distance between the kinks, which then become confined and form mesons.

In the case of two weakly coupled chains, one can treat one chain as a source of a longitudinal magnetic field on the other: for nonoverlapping segments of ground-state configurations, the system is in a "false" ground state. Thus, kink confinement can take place in two different ways, as illustrated in Fig. 3. The energy cost of the region with opposite magnetization for spins on the same rung is proportional to the distance between either a kink and an antikink in the same chain [see Fig. 3(a)], or between two kinks in different chains [see Fig. 3(b)]. The former case of an intrachain bound state between a kink and an antikink is the familiar meson [2]. We shall refer to the latter case as an interchain bound state. Note that, in contrast with mesons, the interchain bound states are topologically charged as they interpolate between two different ground states.
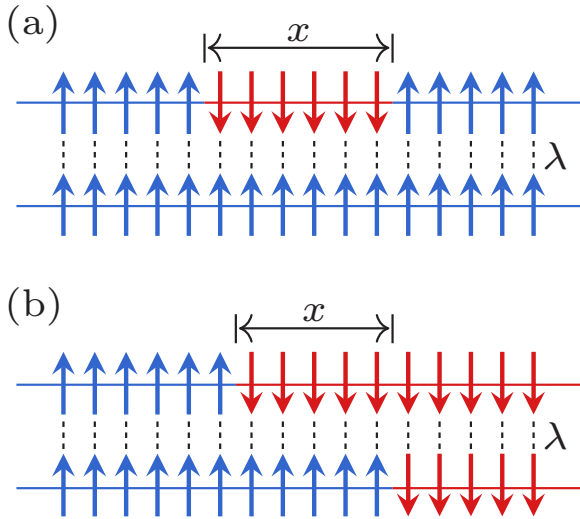
FIG. 3. Schematic representation of the (a) intrachain and (b) interchain mesons on the ferromagnetic two-leg Ising ladder. An effective potential proportional to the separation x between the kinks is induced in the region where the spins are aligned along opposite directions.
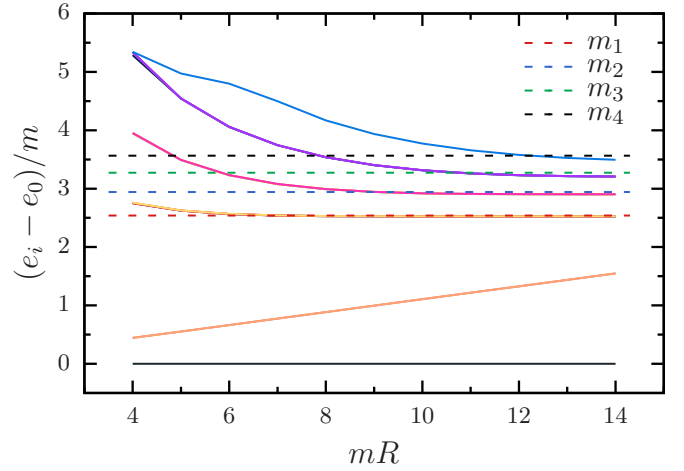

FIG. 4. Finite-size energy gaps in the ferromagnetic phase for $\tilde{\lambda} = 0.03$ from TFSA. The ground state is doubly degenerate (horizontal lines at 0 energy). The lines with fitted slope 0.111 correspond to the two degenerate false vacua. Using the analytical energy density $\chi = 2\lambda \bar{s}^2 \approx 0.112$, we also indicate the meson masses obtained from the semiclassical approximation $m_n \approx 2m - z_n \chi^{2/3}$.

The system can now be modeled by a mean-field Hamiltonian in analogy with the TFIM in a longitudinal field. We write the effective, mean-field two-kink Hamiltonian as [2]

$$H_{2k} = \varepsilon(k_1) + \varepsilon(k_2) + \chi|x_2 - x_1|, \qquad (4)$$

where the dispersions $\varepsilon(k_i)$ are given in Eq. (2), $x_{1,2}$ are the positions of the kinks, and $\chi = 2\lambda\langle\sigma^x\rangle^2$ [56], with $\langle\sigma^x\rangle = (1 - h_z^2)^{1/8}$ being the order parameter of the ferromagnetic TFIM [48].

The Hamiltonian in Eq. (4) was studied in detail in Ref. [4]. In particular, one can use Bohr-Sommerfeld semiclassical quantization to obtain the dispersion relations of the bound states. Using the conservation of the total meson momentum $P = k_1 + k_2$, the problem is reduced to solving the equations [2,4]

$$2E(P, \nu)k - \int_{-k}^{k} dp\, \Omega(p, P) = \pi\chi\left(\nu + \frac{1}{2}\right),$$
$$\Omega(k, P) = E(P, \nu), \qquad (5)$$

where $\Omega(k, P) = \varepsilon(k + P/2) + \varepsilon(k - P/2)$ and $k \in [0, \pi]$. For mesons, i.e., intrachain bound states, the quantum number ν must be an odd integer to obtain antisymmetric wave functions with respect to exchanging the positions of the kinks. This constraint stems from the Pauli exclusion principle for kinks in the same chain. We denote the corresponding meson dispersion relations by $E_n(P) = E(P, \nu = 2n - 1)$, with $n = 1, 2, 3, \dots$. By contrast, there is no such constraint for interchain bound states, in which the kinks carry different leg indices, and symmetric wave functions are allowed. Thus, the quantum number ν can assume any integer values. The dispersion relations for interchain bound states are denoted by $E'_n(P) = E(P, \nu = n - 1)$, with $n = 1, 2, 3, \dots$. Note that $E'_{2n}(P) = E_n(P)$, which means that, within the mean-field approximation of Eq. (4), interchain bound states with an-

tisymmetric wave functions are degenerate with intrachain bound states.

The integral equation in Eqs. (5) can be solved numerically, giving the dispersion relations $E_n(P)$ and $E'_n(P)$. The minimum of each dispersion determines the corresponding particle masses, which we denote by $m_n = E_n(P = 0)$ for mesons and $m'_n = E'_n(P = 0)$ for interchain bound states. The lightest bound state of all is the first interchain one, with mass m'_1. We have checked the predictions of the semiclassical solution by calculating the meson masses using the TFSA. The procedure is the same as for the Ising model in a longitudinal field [1,2]. We report the finite size spectrum in the case of $\tilde{\lambda} = 0.03$ in the ferromagnetic phase in Fig. 4. At small χ and for energies near $2m$, as considered in this figure, the meson masses are well approximated by $m_n = 2m - z_n\chi^{2/3}$, where z_n is the nth zero of the Airy function. Better approximations can be used in the general case, see Refs. [2,3,5,57].

Some comments are in order. For low energies, Eqs. (5) are only valid for sufficiently small values of the total momentum. It breaks down when the second derivative $\partial^2\Omega(k, P)/\partial k^2$ at $k = 0$ becomes negative and the classically allowed regions no longer correspond to the domain of integration used in Eqs. (5) [4]. Moreover, for large values of ν there is no solution to Eqs. (5) because the total momentum cannot be arbitrarily large semiclassically [6]. To circumvent these problems, we consider solutions of the two-body problem on a lattice described by the Hamiltonian

$$H_{2k}^{\text{lat}} = \sum_{j_1, j_2} \sum_{r \geqslant 0} t_r(|j_1 + r, j_2\rangle\langle j_1, j_2| + |j_1, j_2 + r\rangle\langle j_1, j_2|$$
$$+ |j_1, j_2\rangle\langle j_1 + r, j_2| + |j_1, j_2\rangle\langle j_1, j_2 + r|)$$
$$+ \sum_{j_1, j_2} \chi|j_2 - j_1| \, |j_1, j_2\rangle\langle j_1, j_2|, \qquad (6)$$

where j_1 and j_2 denote the positions of the kinks. The parameter χ in the interaction potential is taken from the field

theory, as in Eq. (4), and a small number of nonzero hopping parameters t_r are fixed so as to approximate the exact kink dispersion. The eigenstates of the Hamiltonian in Eq. (6) have wave functions of the form $\langle j_1, j_2 | \Psi \rangle = e^{iP(j_1+j_2)/2} \phi(j_2 - j_1)$, where P is the center-of-mass momentum and $\phi(x)$ is the normalizable wave function for the relative coordinate. Solving the Schrödinger equation for $\phi(x)$ numerically on a finite lattice, we find that this approach is in excellent agreement with the semiclassical solution in the momentum range where Eqs. (5) holds, but it also provides the bound state dispersion relations in the vicinity of $P = \pi$. We will use these dispersion relations to analyze the tDMRG results in Sec. IV B.

IV. DYNAMICAL STRUCTURE FACTORS

We are interested in the DSFs of one- and two-spin operators for the two-leg Ising ladder described by the Hamiltonian in Eq. (1). We focus on the parameter regime deep in the ferromagnetic phase, where the elementary excitations can be pictured as domain walls created in pairs by the σ^z operator. The DSF for the spin operator on leg $\alpha = 1$ is defined as

$$S^{zz}(q, \omega) = \frac{1}{L} \int_{-\infty}^{\infty} dt \, e^{i\omega t} \sum_{j,j'}^{L} e^{-iq(j-j')} C^{zz}(j, j', t), \quad (7)$$

with the time-dependent correlations

$$C^{zz}(j, j', t) = \langle \Psi_0 | \sigma_{1,j}^z(t) \sigma_{1,j'}^z(0) | \Psi_0 \rangle$$
$$- \langle \Psi_0 | \sigma_{1,j}^z | \Psi_0 \rangle \langle \Psi_0 | \sigma_{1,j'}^z | \Psi_0 \rangle. \quad (8)$$

Here, $|\Psi_0\rangle$ is the ground state and $\sigma_{1,j}^z(t) = e^{iHt} \sigma_{1,j}^z e^{-iHt}$ is the operator $\sigma_{1,j}^z$ evolved in real time. We can write $S^{zz}(q, \omega)$ in the Lehmann representation as

$$S^{zz}(q, \omega) = \frac{2\pi}{L} \sum_{l>0} |\langle \Psi_l | \sigma_q^z | \Psi_0 \rangle|^2 \delta(\omega - E_l + E_0), \quad (9)$$

where $\sigma_q^z = \sum_j e^{-iqj} \sigma_{1,j}^z$, $|\Psi_l\rangle$ are eigenstates of H with energy E_l, and E_0 is the ground-state energy. In the weak coupling regime, $0 < \lambda \ll 1$, we expect $S^{zz}(q, \omega)$ to be dominated by excited states in which two kinks created in leg $\alpha = 1$ form an intrachain meson with total momentum $P = q$.

For two-spin operators, we consider two distinct DSFs defined as

$$S_{\text{sl/dl}}^{4z}(q, \omega) = \frac{1}{L} \int_{-\infty}^{+\infty} dt \, e^{i\omega t} \sum_{j,j'}^{L} e^{-iq(j-j')} C_{\text{sl/dl}}^{4z}(j, j', t),$$
$$(10)$$

where

$$C_{\text{sl/dl}}^{4z}(j, j', t) = \langle \Psi_0 | O_j^{\text{sl/dl}}(t) O_{j'}^{\text{sl/dl}}(0) | \Psi_0 \rangle$$
$$- \langle \Psi_0 | O_j^{\text{sl/dl}} | \Psi_0 \rangle \langle \Psi_0 | O_{j'}^{\text{sl/dl}} | \Psi_0 \rangle \quad (11)$$

are the time-dependent correlation functions for the operators

$$O_j^{\text{sl}} = \sigma_{1,j}^z \sigma_{1,j+2}^z, \quad (12)$$

$$O_j^{\text{dl}} = \sigma_{1,j}^z \sigma_{2,j}^z. \quad (13)$$

The labels sl and dl in Eqs. (10)–(13) indicate that the operators act on two sites located in the same leg or different legs,

respectively. The DSFs $S_{\text{sl/dl}}^{4z}(q, \omega)$ admit spectral decompositions analogous to Eq. (9). In a simple classical picture of the ferromagnetic phase, the action of O_j^{sl} on the fully polarized state creates four domain walls in the same chain. On the other hand, O_j^{dl} creates two domain walls in each chain. We then expect these DSFs to have significant spectral weight associated with four-kink excitations, which form two mesons or two interchain bound states for $0 < \lambda \ll 1$. Note, however, that two-kink excitations are also allowed by selection rules. They are in fact present as contributions in which the four-point function in Eq. (11) factorizes into two-point functions, due to the nonzero expectation value of the σ^z operator for $h_z \neq 0$.

Since the Ising ladder is nonintegrable, we have used the adaptive tDMRG [41] to compute the DSFs of open ladders. While this method is most efficient at treating one-dimensional systems with nearest-neighbor interactions, it is also possible to use tDMRG to investigate narrow ladders. To do so, we enlarge the local Hilbert space by combining the rung sites into a supersite, so the Suzuki-Trotter decomposition can be applied exactly in the nonrenormalized DMRG sites.

To investigate the effects of a weak interchain coupling on the energy spectrum, we will discuss the cases of $\lambda = 0$ and $\lambda = 0.1$. Our tDMRG results were obtained by setting the ladder length $L = 160$ and the transverse magnetic field $h_z = 0.5$. The time-dependent correlations were computed by keeping up to 200 states per DMRG block. The temporal Fourier transforms in Eqs. (7) and (10) were performed in the time interval $-t_{\max} < t < t_{\max}$, where $t_{\max}$ is maximum time obtained by tDMRG. To set the maximum time, we have to take into account two limitations. The first one is due to the finite length of the ladder. Since we are not interested in boundary effects, $t_{\max}$ is such that the propagation of the correlations does not reach the edges of the chains, i.e., $t_{\max} < L/(2v)$, where v is the maximal velocity that defines the light cone. The second limitation is the numerical errors generated by the truncation procedure and the order of the Suzuki-Trotter decomposition. In our computations, the error related to the truncation procedure is smaller than 10^{-7} and the time evolution was carried out with second-order Suzuki-Trotter decomposition using a time step $\delta t = 0.1$. The maximum time we have considered is in the interval $t_{\max} \in [50, 90]$. We present our numerical results in the following.

A. Decoupled chains

Let us first discuss the integrable case $\lambda = 0$, corresponding to two decoupled TFIMs. The energy spectrum of the system can be completely understood from the dispersion relation of free kinks in Eq. (2). In Fig. 5, we show the region in the (q, ω) plane associated with two- and four-kink excitations, which determine the support of $S^{zz}(q, \omega)$ and $S_{\text{sl/dl}}^{4z}(q, \omega)$. Note that the two-kink continuum starts off at $\Delta = 2m = 4J(1 - h_z)$, whereas the four-particle continuum starts at 2Δ. The width of the continua depends on the bandwidth of the kink dispersion, which is governed by the transverse field. The upper threshold of the two-kink continuum is given by $\Omega_{2,u}(q) = 2\varepsilon(\pi - q/2)$ and the lower threshold of the four-kink continuum by $\Omega_{4,l}(q) = 4\varepsilon(q/4)$. Thus, we could
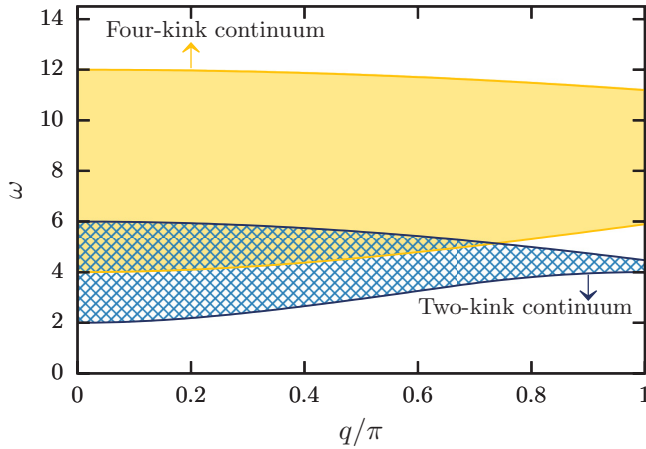
FIG. 5. Two- and four-kink excitation continua of the decoupled Ising ladder with $h_z = 0.5$. The energies are measured in units of $J = 1$. The area in blue (yellow) corresponds to the continuum of two (four) kinks. The solid lines indicate the lower and upper thresholds of the continua.

avoid their overlap by requiring $\Omega_{4,1}(0) > \Omega_{2,u}(0)$, which is verified for $h_z < 1/3$. However, a smaller h_z also implies narrower bands for the kinks and slower dynamics. This requires longer simulation times, making the computation of the DSFs unpractical from the tDMRG point of view. Hereafter we shall consider $h_z = 0.5$, as illustrated in Fig. 5. In this case, the two- and four-kink continua overlap for momentum $q < q_0 \approx 0.74\pi$ but they are separated by a gap for $q > q_0$.

In Fig. 6, we show the DSFs computed by tDMRG for $\lambda = 0$ and $h_z = 0.5$. The support of $S^{zz}(q, \omega)$ is precisely the two-kink continuum shown in Fig. 5. By contrast, the DSFs $S^{4z}_{sl/dl}(q, \omega)$ exhibit two- and four-kink contributions (see Figs. 6 and 7). Despite the different spectral weight distributions, $S^{4z}_{dl}(q, \omega)$ and $S^{4z}_{sl}(q, \omega)$ display the same support, with a significant weight above the two-kink continuum. Note the clear separation between the two- and four-kink continua at $q = \pi$.

B. Weakly coupled chains

We now consider a weak interchain coupling $\lambda = 0.1$. This coupling introduces an effective linear potential that confines the kinks of the Ising chains into bound states. As a result, the two-kink continuum must break up into a series of single-meson peaks. On the other hand, the four-kink continuum probed by the two-spin DSFs may turn into a continuum of two propagating bound states but it may also give rise to two-meson bound states. Moreover, in the two-leg ladder we can have both mesons and interchain bound states, and the latter should only be revealed in the DSF $S^{4z}_{dl}(q, \omega)$.

The signatures of the mesons can be directly observed in the DSF of the one-spin operator. Indeed, in Fig. 8 we see a discrete energy spectrum related to the excitations created by one spin flip. Our numerical results show a remarkable agreement with the meson dispersion relations calculated as discussed in Sec. III, even in the regime where the semiclassical approximation breaks down. The inset of Fig. 8 shows the line shape of $S^{zz}(q, \omega)$ for $q = 0$, where we compare the
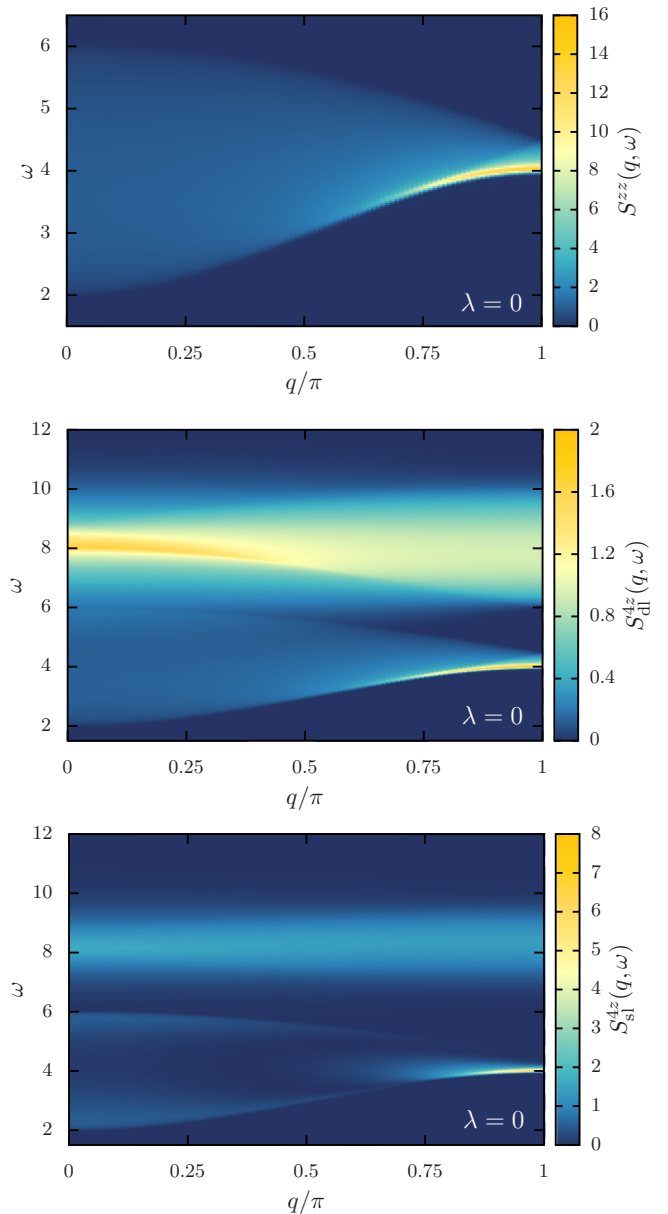

FIG. 6. DSFs for the decoupled two-leg Ising ladder with $h_z = 0.5$, as a function of q and ω. The top panel shows the one-spin DSF $S^{zz}(q, \omega)$, whose support corresponds to the two-kink continuum. The two-spin DSFs $S^{4z}_{dl}(q, \omega)$ (middle) and $S^{4z}_{sl}(q, \omega)$ (bottom) contain two-kink and four-kink contributions.

peak frequencies with the predicted meson masses m_n. Note that the frequency resolution is limited by the finite time t_{max} reached by tDMRG, which accounts for the finite width of the meson peaks.

To interpret our numerical results for $S^{4z}_{dl}(q, \omega)$, let us first discuss the case of an open ladder with only one kink in each leg. In this case, the kinks are confined due to the linear potential associated with the region where the chains present opposite local magnetization, as shown in Fig. 3(b). These confined states are interchain bound states. As discussed in Sec. III, now the two-kink wave function is not required to be antisymmetric, because the kinks are distinguished by their leg degree of freedom. Thus, we also take into account the
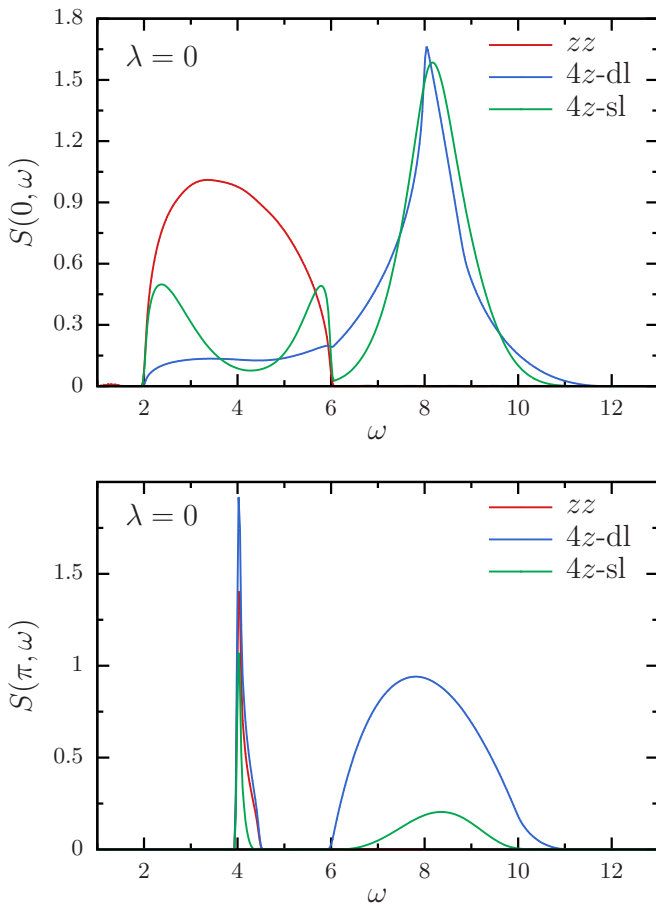
FIG. 7. Constant-momentum cuts of the one-spin and two-spin DSFs for $\lambda = 0$ and $h_z = 0.5$. The top and bottom panels show the line shapes for $q = 0$ and $q = \pi$, respectively. The two- and four-kink continua overlap for $q = 0$, but they are separated by an energy gap $\Delta_\pi = \Omega_{4,1}(\pi) - \Omega_{2,\mathrm{u}}(\pi) \approx 1.42$ for $q = \pi$.
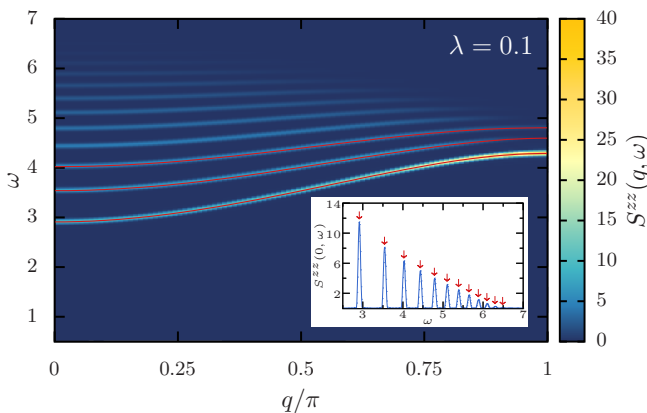

FIG. 8. One-spin DSF for $\lambda = 0.1$ and $h_z = 0.5$, as a function of q and ω. The solid red lines represent the dispersion relations of the intrachain bound states, i.e., mesons, extracted from the solution of the two-kink problem on the lattice. The inset shows the line shape of $S^{zz}(q, \omega)$ for $q = 0$. The red arrows indicate the masses m_n for the first 12 mesons.
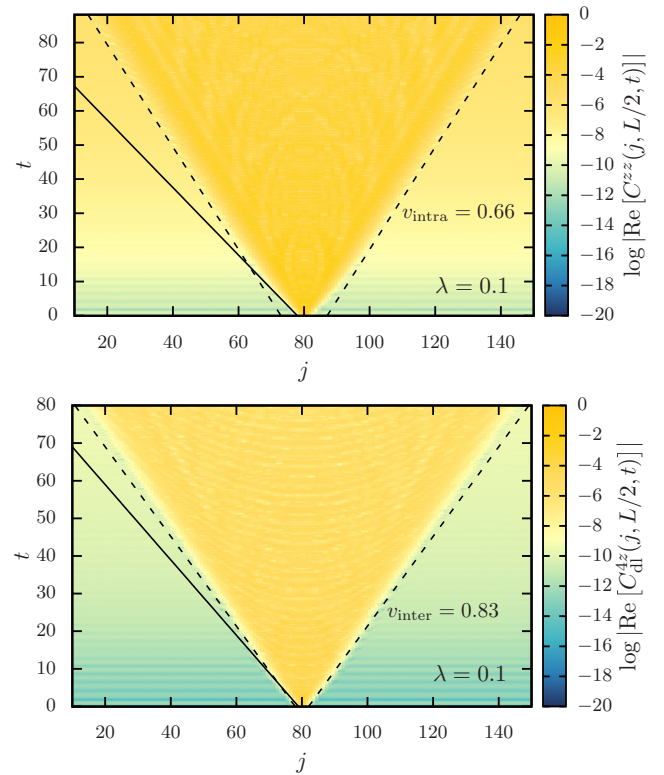

FIG. 9. Real part of the time-dependent correlations $C^{zz}(j, L/2, t)$ (top) and $C_{\mathrm{dl}}^{4z}(j, L/2, t)$ (bottom) as a function of j and t. The solids lines are straight lines whose slope is the maximal kink velocity $v_{\mathrm{kink}} = 2h_z = 1$. The dashed lines are straight lines with slope v_{intra} for $C^{zz}(j, L/2, t)$ and v_{inter} for $C_{\mathrm{dl}}^{4z}(j, L/2, t)$. The values of v_{intra} and v_{inter} were acquired from the bound state dispersion relations.

symmetric solutions. An important feature is that the first (lightest) interchain bound state has lower energy and higher velocity than the lightest meson. Note that single interchain bound states do not exist in ladders with periodic boundary conditions, nor in the bulk spectrum of open ladders, because local operators can only create pairs of kinks in one or both legs. In particular, the DSF $S_{\mathrm{dl}}^{4z}(q, \omega)$ must contain contributions from excited states with at least two interchain bound states. However, one can still detect interchain bound states by analyzing the propagation of perturbations in the time-dependent correlations as well as the lower threshold of the two-particle continuum.

In Fig. 9, we show the time-dependent correlations $C^{zz}(j, L/2, t)$ and $C_{\mathrm{dl}}^{4z}(j, L/2, t)$. To check whether the maximal velocities of the bound states coincide with the ones that bound the light cones, we have computed the dispersions following the procedure described previously. Recall that the dispersion $E_1'(P)$ of the lightest interchain bound state is calculated by taking the symmetric ground state wavefunction in the diagonalization of the Hamiltonian in Eq. (6). For $h_z = 0.5$ and $\lambda = 0.1$, we find that the maximal intrachain- and interchain-bound-state velocities are $v_{\mathrm{intra}} \approx 0.66$ and $v_{\mathrm{inter}} \approx 0.83$. As expected, our results indicate that the fastest particle observed in $C^{zz}(j, L/2, t)$ and $C_{\mathrm{dl}}^{4z}(j, L/2, t)$ are the lightest meson and interchain bound states, respectively.
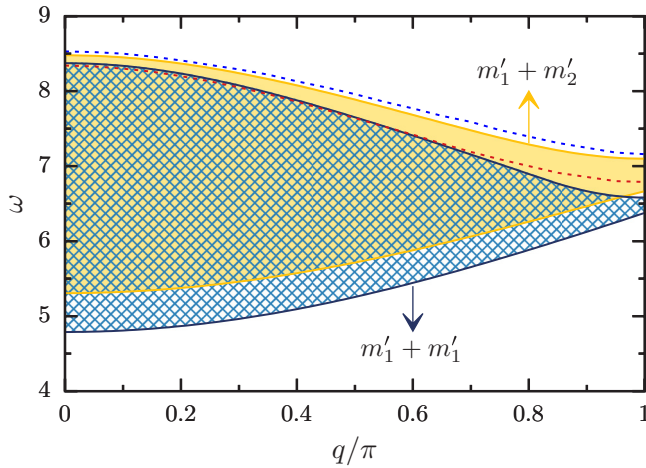
FIG. 10. Excitations with two interchain bound states in the two-leg Ising ladder for $\lambda = 0.1$ and $h_z = 0.5$, calculated using the bound state dispersion relations. The area in blue and yellow represent the continua for $m_1' + m_1'$ and $m_1' + m_2'$ excitations, respectively. The dashed lines near the upper thresholds of the continua are extracted from the bright lines in the tDMRG results for $S_{\mathrm{dl}}^{4z}(q, \omega)$ in Fig. 11.

Another way to identify the interchain bound state is to look at the continuum of excitations in $S_{\mathrm{dl}}^{4z}(q, \omega)$. Since the dispersion of the lightest interchain bound state is below the intrachain ones, the lower threshold of the continuum must correspond to scattering states of two lightest interchain bound states. Similar to our analysis of the two-kink continuum in the decoupled case, we can use the bound-state dispersions to construct the two-particle continua. We label them by the corresponding masses: here, $m_{n_1}' + m_{n_2}'$, with $n_1, n_2 \geqslant 1$, denotes the continuum defined by one interchain bound state with dispersion $E_{n_1}'(P)$ and another one with dispersion $E_{n_2}'(P)$. Note that there is no upper threshold in the total two-bound-state continuum, and the separation between different $m_{n_1}' + m_{n_2}'$ continua is not sharply defined once they overlap and the bound states can decay into lighter particles. Nevertheless, this classification will prove useful in the interpretation of the two-spin DSFs.

The $m_1' + m_1'$ and $m_1' + m_2'$ continua are represented in Fig. 10. The lowest excitation occurs at the frequency $\omega = 2m_1'$, corresponding to the energy cost of creating two interchain bound states with momentum $q = 0$. For $\lambda = 0.1$ and $h_z = 0.5$, we find $m_1' = E_1'(0) \approx 2.39$. This mass is consistent with the lower threshold of the continuum present in the DSF $S_{\mathrm{dl}}^{4z}(q, \omega)$ calculated by tDMRG (see Fig. 11). At $q = 0$, the peaks that appear below and slightly above $2m_1'$ can be identified with single-meson excitations, which descend from the two-kink continuum and have the same frequencies observed in $S^{zz}(q, \omega)$. Remarkably, for all values of q the spectral weight associated with the excitation of two bound states vanishes as the frequency approaches the lower threshold of the $m_1' + m_1'$ continuum, and there is no evidence for a bound state of two interchain bound states below the continuum.

A prominent feature in the line shape of the DSF $S_{\mathrm{dl}}^{4z}(q, \omega)$ for $q = 0$, see the bottom panel in Fig. 11, is the steep rise in the intensity as the frequency increases above $2m_1'$, terminating in a highly asymmetric peak near the upper
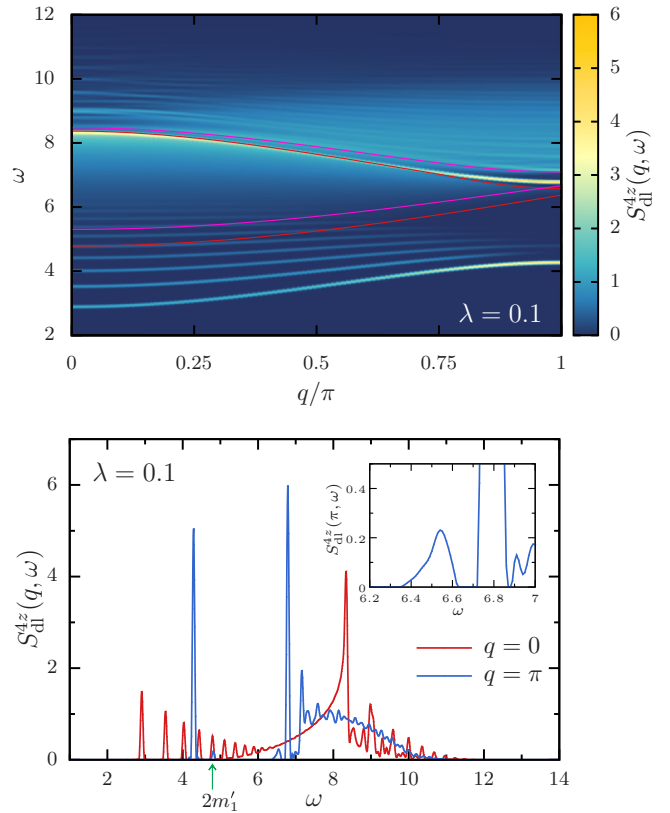

FIG. 11. Top: Two-spin DSF $S_{\mathrm{dl}}^{4z}(q, \omega)$ for $\lambda = 0.1$ and $h_z = 0.5$, as a function of q and ω. The solid red lines are the lower and upper thresholds of the two-interchain-bound-state continuum $m_1' + m_1'$. The pink lines are the thresholds of the continuum $m_1' + m_2'$. Bottom: Constant-momentum cuts of the DSF at $q = 0$ and $q = \pi$. The green arrow indicates the lower threshold of the continuum for $q = 0$, given by twice the mass of the lightest interchain bound state. For $q = \pi$, there is a pronounced peak above the $m_1' + m_1'$ continuum. The inset is a zoom in of a frequency interval around this peak. The predictions for the lower and upper thresholds of the $m_1' + m_1'$ continuum at $q = \pi$ are $\omega \approx 6.38$ and $\omega \approx 6.58$, respectively.

threshold of the $m_1' + m_1'$ continuum. By contrast, for $q = \pi$ the $m_1' + m_1'$ continuum covers only a narrow frequency range, in agreement with the result in Fig. 10, and has a rather small spectral weight. However, we observe a sharp peak *above* the $m_1' + m_1'$ continuum. The amplitude of this peak is even higher than that of the first meson peak in $S_{\mathrm{dl}}^{4z}(q = \pi, \omega)$. To track the evolution of the new peak, in Fig. 12 we show the line shapes of $S_{\mathrm{dl}}^{4z}(q, \omega)$ for different values of momentum. As one moves from $q = 0$ to $q = \pi$, the peak appears to split off from the continuum below it. For this reason, and because the width is within the frequency resolution of the tDMRG simulations, we interpret this peak as a bound state of two interchain bound states.

On general grounds, we expect mesons to interact via a short-range potential, since, unlike the linear potential responsible for kink confinement, the interaction energy does not increase with the distance between mesons. The same is true for interchain bound states in the two-leg ladder. The presence of a bound state of two interchain bound states, or rather an *antibound* state, above the $m_1' + m_1'$ continuum
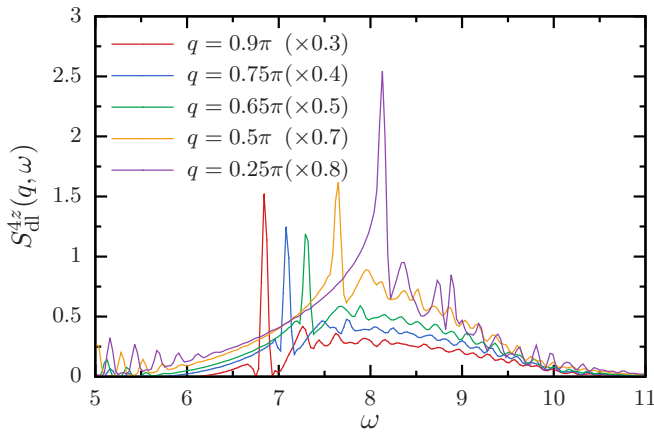
FIG. 12. Line shape of $S_{\mathrm{dl}}^{4z}(q,\omega)$ for $\lambda = 0.1$, $h_z = 0.5$, and five different values of q. As q increases, a narrow peak emerges from the $m_1' + m_1'$ continuum below it.

FIG. 13. Real part of the time-dependent correlation $C_{\mathrm{sl}}^{4z}(j, L/2, t)$ as a function of j and t. The solid and dashed lines are straight lines with slope $v_{\mathrm{kink}} = 1$ and $v_{\mathrm{intra}} = 0.66$, respectively.

suggests that their interaction is predominantly repulsive. The effective scattering amplitude in the Bethe-Salpeter equation that describes the bound-state formation must be a function of the momenta of the interchain bound states, and also depend on the internal wave function $\phi(x)$ for the relative coordinates between kinks, but we do not attempt to calculate it here. It is important to note that the formation of bound states of bound states should not be restricted to the $m_1' + m_1'$ continuum, but may occur for all $m_{n_1}' + m_{n_2}'$ excitations. Thus, one possible explanation for the irregular line shape of $S_{\mathrm{dl}}^{4z}(q,\omega)$ above the $m_1' + m_1'$ continuum is that it stems from a series of overlapping two-particle continua and the associated bound states with finite lifetimes. This is consistent with a second peak found just above the $m_1' + m_2'$ continuum, see Figs. 10 and 11.

Finally, let us discuss the tDMRG results for $S_{\mathrm{sl}}^{4z}(q,\omega)$. In contrast to $S_{\mathrm{dl}}^{4z}(q,\omega)$, the spectrum of $S_{\mathrm{sl}}^{4z}(q,\omega)$ does not contain interchain bound states because the two spin flips are performed on the same leg. For this reason, only the antisymmetric wave functions are allowed in the solutions of Eqs. (5) and (6). Indeed, from the propagation of the time-dependent correlation shown in Fig. 13, we confirm that the fastest particle in this case is the lightest intrachain bound state with maximal velocity $v_{\mathrm{intra}} \approx 0.66$.

Figure 14 shows the results for $S_{\mathrm{sl}}^{4z}(q,\omega)$. The first remark is that this DSF also exhibits single-meson peaks at the same frequencies as the one-spin DSF. However, in this case the amplitude of the meson peaks for $q = 0$ is a nonmonotonic function of frequency, behaving similarly to the two-kink contribution in $S_{\mathrm{sl}}^{4z}(q=0,\omega)$ for the decoupled ladder (see Fig. 7). In addition, the lower threshold of the two-meson continuum at $\omega = 2m_1$ is not apparent in the line shape for $q = 0$. The reason is that the spectral weight vanishes more rapidly than in the case of $S_{\mathrm{dl}}^{4z}(q,\omega)$ as the frequency approaches the lower threshold of the $m_1 + m_1$ continuum. This was already noticeable in the DSF for decoupled chains in Fig. 7 and follows from the stronger effect of the Pauli exclusion principle when all four kinks propagate in the same leg. Also in Fig. 14, we show the line shape of $S_{\mathrm{sl}}^{4z}(q,\omega)$ for $q = \pi$. Again, we observe a series of peaks above the upper
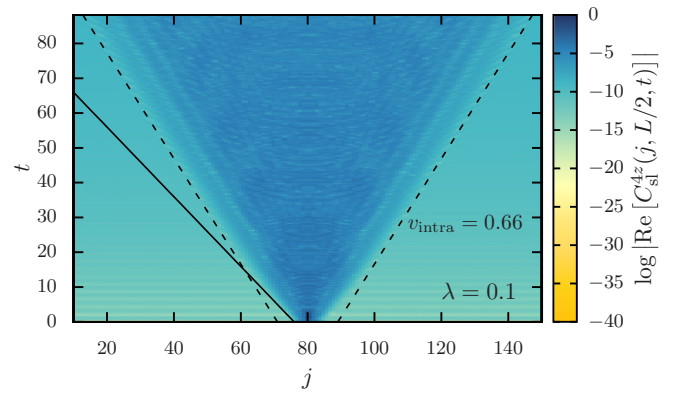
thresholds of the $m_{n_1} + m_{n_2}$ continua and attribute them to bound states of two mesons with finite lifetimes. The multiple peaks can be discerned more clearly in this case as they are more widely separated than in $S_{\mathrm{dl}}^{4z}(q,\omega)$, since here we have only half as many continua of two propagating bound states.
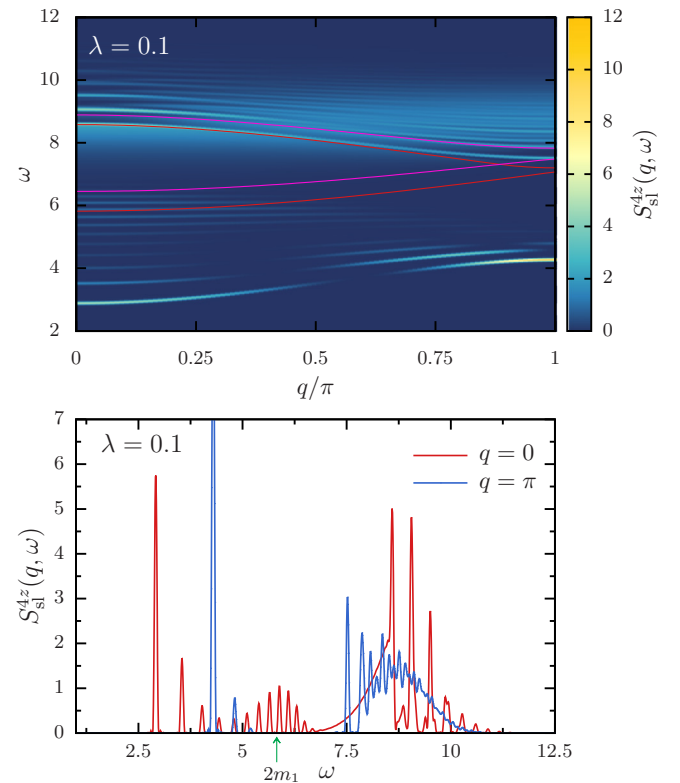

FIG. 14. Top: Two-spin DSF $S_{\mathrm{sl}}^{4z}(q,\omega)$ as a function of q and ω. The solid red lines are the thresholds of the $m_1 + m_1$ continuum. The pink lines are the thresholds of the $m_1 + m_2$ continuum. Bottom: Line shapes of $S_{\mathrm{sl}}^{4z}(q,\omega)$ for $q = 0$ and $q = \pi$. The green arrow at $\omega = 2m_1$ marks the lower threshold of the two-meson continuum for $q = 0$.

V. CONCLUSIONS

We have studied the formation of intra- and interchain bound states in the ferromagnetic phase of the transverse-field two-leg Ising ladder. First, we mapped out the phase diagram of the model using DMRG and analyzed the critical line using the scaling field theory and the truncated fermionic space approach. We then used the adaptive tDMRG method to calculate three different DSFs. The one-spin DSF probes excitations with two domain walls, or kinks, in the same leg of the two-leg Ising ladder. The other two DSFs, defined for two-spin operators, probe excitations with four kinks, either all in the same leg or two pairs in different legs.

The spectrum of the one-spin operator is completely described by the confinement of kinks and antikinks into single mesons. A family of excitations, which we call interchain bound states, appears in the spectrum of the two-spin operator acting on both legs. The lightest interchain bound state has a smaller mass than the lightest meson because its wave function is not required to vanish when the two kinks are in the same rung, but in different legs. As a consequence, the interchain bound states determine the lower threshold of the two-particle continuum. The two-spin DSFs also exhibit a series of higher-energy peaks associated with bound states of bound states, which are two-meson bound states in the case where spin operators act on sites within the same chain.

Our results should be relevant to the interpretation of experiments on weakly coupled Ising chains. In fact, the existence of a hierarchy of bound states was proposed based on the experiments reported in Ref. [16]. It would be interesting to quantify the contribution from different two-spin operators to the absorption spectra measured by terahertz spectroscopy and investigate the role of the two-meson continuum and of the interchain bound states.

Finally, we would like to briefly comment on the generalization of our results to N-leg ladders and three-dimensional arrays of weakly coupled chains, as found in real materials.

The interchain bound state can be generalized to bound states of N kinks, but creating them with a significant amplitude requires an operator that acts simultaneously on N spins in different chains. The resulting excitation can be interpreted as a domain wall whose energy increases with N. On the other hand, we may consider the fate of interchain bound states composed of two kinks or two antikinks when we increase the number of coupled chains. In this case, the neighboring chains which are not excited introduce a linear potential that confines pairs of interchain bound states with opposite topological charges. As a result, while the two-meson continuum survives in the presence of more chains, we expect the continuum of two interchain bound states to be completely replaced by bound states of bound states.

Note added. Recently, we became aware of a related work by Lagnese *et al.* [58], who independently developed the idea of intrachain and interchain bound states in a different ladder system.

[1] B. M. McCoy and T. T. Wu, Phys. Rev. D **18**, 1259 (1978).

[2] P. Fonseca and A. Zamolodchikov, arXiv:hep-th/0612304.

[3] S. B. Rutkevich, Phys. Rev. Lett. **95**, 250601 (2005).

[4] S. B. Rutkevich, J. Stat. Phys. **131**, 917 (2008).

[5] S. B. Rutkevich, J. Phys. A: Math. Theor. **42**, 304025 (2009).

[6] M. Kormos, M. Collura, G. Takács, and P. Calabrese, Nat. Phys. **13**, 246 (2017).

[7] P. P. Mazza, G. Perfetto, A. Lerose, M. Collura, and A. Gambassi, Phys. Rev. B **99**, 180302(R) (2019).

[8] R. Verdel, F. Liu, S. Whitsitt, A. V. Gorshkov, and M. Heyl, arXiv:1911.11382.

[9] A. J. A. James, R. M. Konik, and N. J. Robinson, Phys. Rev. Lett. **122**, 130603 (2019).

[10] A. Lerose, F. M. Surace, P. P. Mazza, G. Perfetto, M. Collura, and A. Gambassi, arXiv:1911.07877 [cond-mat.stat-mech].

[11] R. J. V. Tortora, P. Calabrese, and M. Collura, arXiv:2005.01679 [cond-mat.stat-mech].

[12] N. Ishimura and H. Shiba, Prog. Theor. Phys. **63**, 743 (1980).

[13] H. Shiba, Prog. Theor. Phys. **64**, 466 (1980).

[14] B. Lake, A. M. Tsvelik, S. Notbohm, D. Alan Tennant, T. G. Perring, M. Reehuis, C. Sekar, G. Krabbes, and Büchner, Nat. Phys. **6**, 50 (2010).

[15] R. Coldea, D. A. Tennant, E. M. Wheeler, E. Wawrzynska, D. Prabhakaran, M. Telling, K. Habicht, P. Smeibidl, and K. Kiefer, Science **327**, 177 (2010).

[16] C. M. Morris, R. Valdés Aguilar, A. Ghosh, S. M. Koohpayeh, J. Krizan, R. J. Cava, O. Tchernyshyov, T. M. McQueen, and N. P. Armitage, Phys. Rev. Lett. **112**, 137403 (2014).

[17] J. A. Kjäll, F. Pollmann, and J. E. Moore, Phys. Rev. B **83**, 020407(R) (2011).

[18] B. Grenier, S. Petit, V. Simonet, E. Canévet, L.-P. Regnault, S. Raymond, B. Canals, C. Berthier, and P. Lejay, Phys. Rev. Lett. **114**, 017201 (2015).

[19] Q. Faure, S. Takayoshi, S. Petit, V. Simonet, S. Raymond, L.-P. Regnault, M. Boehm, J. S. White, M. Mansson, C. Rüegg, P. Lejay, B. Canals, T. Lorenz, S. C. Furuya, T. Giamarchi, and B. Grenier, Nat. Phys. **14**, 716 (2018).

[20] Z. Wang, M. Schmidt, A. Loidl, J. Wu, H. Zou, W. Yang, C. Dong, Y. Kohama, K. Kindo, D. I. Gorbunov, S. Niesen,

O. Breunig, J. Engelmayer, and T. Lorenz, Phys. Rev. Lett. **123**, 067202 (2019).

[21] Z. Wang, M. Schmidt, A. K. Bera, A. T. M. N. Islam, B. Lake, A. Loidl, and J. Deisenhofer, Phys. Rev. B **91**, 140404(R) (2015).

[22] A. K. Bera, B. Lake, F. H. L. Essler, L. Vanderstraeten, C. Hubig, U. Schollwöck, A. T. M. N. Islam, A. Schneidewind, and D. L. Quintero-Castro, Phys. Rev. B **96**, 054423 (2017).

[23] W. J. Gannon, I. A. Zaliznyak, L. S. Wu, A. E. Feiguin, A. M. Tsvelik, F. Demmel, Y. Qiu, J. R. D. Copley, M. S. Kim, and M. C. Aronson, Nat. Commun. **10**, 1123 (2019).

[24] F. Liu, R. Lundgren, P. Titum, G. Pagano, J. Zhang, C. Monroe, and A. V. Gorshkov, Phys. Rev. Lett. **122**, 150601 (2019).

[25] A. Lerose, B. Žunkovič, A. Silva, and A. Gambassi, Phys. Rev. B **99**, 121112(R) (2019).

[26] W. L. Tan, P. Becker, F. Liu, G. Pagano, K. S. Collins, A. De, L. Feng, H. B. Kaplan, A. Kyprianidis, R. Lundgren, W. Morong, S. Whitsitt, A. V. Gorshkov, and C. Monroe, arXiv:1912.11117.

[27] M. Fava, R. Coldea, and S. A. Parameswaran, arXiv:2004.04169 [cond-mat.str-el].

[28] G. Magnifico, M. Dalmonte, P. Facchi, S. Pascazio, F. V. Pepe, and E. Ercolessi, Quantum **4**, 281 (2020).

[29] T. Chanda, J. Zakrzewski, M. Lewenstein, and L. Tagliacozzo, Phys. Rev. Lett. **124**, 180602 (2020).

[30] D. Porras and J. I. Cirac, Phys. Rev. Lett. **92**, 207901 (2004).

[31] J. G. Bohnet, B. C. Sawyer, J. W. Britton, M. L. Wall, A. M. Rey, M. Foss-Feig, and J. J. Bollinger, Science **352**, 1297 (2016).

[32] M. Marcuzzi, J. Minář, D. Barredo, S. de Léséleuc, H. Labuhn, T. Lahaye, A. Browaeys, E. Levi, and I. Lesanovsky, Phys. Rev. Lett. **118**, 063606 (2017).

[33] P. Jurcevic, H. Shen, P. Hauke, C. Maier, T. Brydges, C. Hempel, B. P. Lanyon, M. Heyl, R. Blatt, and C. F. Roos, Phys. Rev. Lett. **119**, 080501 (2017).

[34] J. Zhang, G. Pagano, P. W. Hess, A. Kyprianidis, H. Kaplan, A. V. Gorshkov, Z.-X. Gong, and C. Monroe, Nature **551**, 601 (2017).

[35] J. Vovrosh and J. Knolle, arXiv:2001.03044 [cond-mat.str-el].

[36] M. W. Haverkort, Phys. Rev. Lett. **105**, 167404 (2010).

[37] L. J. P. Ament, M. van Veenendaal, T. P. Devereaux, J. P. Hill, and J. van den Brink, Rev. Mod. Phys. **83**, 705 (2011).

[38] A. C. Potter, T. Senthil, and P. A. Lee, Phys. Rev. B **87**, 245106 (2013).

[39] S. R. White, Phys. Rev. Lett. **69**, 2863 (1992).

[40] P. Fonseca and A. Zamolodchikov, J. Stat. Phys. **110**, 527 (2003).

[41] S. R. White and A. E. Feiguin, Phys. Rev. Lett. **93**, 076401 (2004).

[42] S. Sachdev, *Quantum Phase Transitions* (Cambridge University Press, Cambridge, 2011).

[43] A. Zamolodchikov, arXiv:1310.4821.

[44] G. Delfino and G. Mussardo, Nucl. Phys. B **516**, 675 (1998).

[45] J. C. Xavier and F. C. Alcaraz, Phys. Rev. B **84**, 094410 (2011).

[46] J. C. Xavier and F. B. Ramos, J. Stat. Mech.: Theory Exp (2014) P10034.

[47] P. Di Francesco, P. Mathieu, and D. Sénéchal, *Conformal Field Theory* (Springer-Verlag, Berlin, 1997).

[48] T. T. Wu, B. M. McCoy, C. A. Tracy, and E. Barouch, Phys. Rev. B **13**, 316 (1976).

[49] A. LeClair, A. Ludwig, and G. Mussardo, Nucl. Phys. B **512**, 523 (1998).

[50] M. Fabrizio, A. O. Gogolin, and A. A. Nersesyan, Nucl. Phys. B **580**, 647 (2000).

[51] Z. Bajnok, L. Palla, G. Takács, and F. Wágner, Nucl. Phys. B **601**, 503 (2001).

[52] G. Feverati, K. Graham, P. A. Pearce, G. Z. Tóth, and G. Watts, J. Stat. Mech.: Theory Exp (2008) P03011.

[53] P. Giokas and G. Watts, arXiv:1106.2448 [hep-th].

[54] M. Lencses and G. Takacs, J. High Energy Phys. 09 (2014) 052.

[55] M. Hogervorst, S. Rychkov, and B. C. van Rees, Phys. Rev. D **91**, 025005 (2015).

[56] Note that, on a single chain, there is only $\langle\sigma\rangle$ in the formula for χ. Here, it is squared due to the mean-field approximation.

[57] M. Lencses and G. Takacs, J. High Energy Phys. 09 (2015) 146.

[58] G. Lagnese, F. M. Surace, M. Kormos, and P. Calabrese, arXiv:2005.03131 [cond-mat.stat-mech].